

New Insights into Structural Evolution of LiNiO₂ Revealed by Operando Neutron Diffraction

Po-Hsiu Chien,^[a] Xianyang Wu,^[a, b, c] Bohang Song,^[a] Zhijie Yang,^[d] Crystal K. Waters,^[d] Michelle S. Everett,^[a] Feng Lin,^[d] Zhijia Du,^{*[b]} and Jue Liu^{*[a]}

LiNiO₂ (LNO) represents the end member in the compositional space of the LiNi_{1-x,y}Mn_xCo_yO₂ (as x and y approach zero) cathode system. Despite its high theoretical specific capacity (275 mAh/g), LNO suffers from phase transitions with large volume change and unfavorable reactions upon electrochemical cycling, which restricts its practical use in the application of lithium-ion batteries. While the contributing factor to the structural instability is commonly linked to the undesired volume collapse associated with the H2-H3 phase transition, detailed analysis of structural evolution following the entire

route of phase transitions (H1-M-H2-H3) in real time under battery operating conditions remains a challenging task. In this work, we employ operando neutron diffraction to study the structural changes (crystal lattice, Li/Ni–O bond length, O–Ni–O bond angles, and LiO₂/NiO₂ layer thickness) of LNO cathode in a home-built Li_xNiO₂ | graphite full cell during Li⁺ de-/intercalation. In particular, the anomalous increase(decrease) of Ni–O(Li–O) bond length at high SOC (> ~85%) in the H3 phase is discussed in the context of O²⁻ (2p)→Ni⁴⁺(3d) negative charge transfer.

1. Introduction

The relentless advancement of Li-Ion Batteries (LIBs) technologies stems from the unquenchable demand for higher energy density as the practical application of interest shifts gradually from portable devices to electric vehicles (EVs)^[1,2] to large-scale grids.^[3] Since the first report of LiNiO₂ (LNO) in 1954,^[4] research efforts have been devoted to assessing the potential of LNO as a cathode material for LIBs.^[5,6] In addition to high theoretical capacity (275 mAh/g), layered LNO, which is isostructural to LiCoO₂ cathode,^[7] is more economically affordable since nickel has a higher natural abundance than cobalt. However, the hindrance LNO faces prior to commercial use lies in the structural instability,^[8,9] which is fundamentally governed by the degree of Li⁺/Ni²⁺ mixing^[10] and Li⁺/vacancy ordering.^[11]

Hence, concerns have been expressed about its electrochemical^[12–14] and thermal^[15,16] performance especially at high degrees of delithiation (> 4.3 V vs. Li/Li⁺). Although extensive works^[17,18] have shown that cation-substituted Ni-rich cathodes, e.g., LiNi_{1-x,y}Mn_xCo_yO₂ (1-x-y≥0.8), can improve the structural/thermal stability and cyclability, the renaissance of research interest in LiNiO₂ has been underway,^[19–23] to meet the harsher criteria for EVs batteries.^[1,2]

Among the challenges such as parasitic surface reactions^[24,25] and formation of disordered rock-salt (NiO) impurity^[26,27] at high state-of-charge (SOC), the sequential phase transition (H1-M-H2-H3)^[28,29] might play a more profound role in altering the structural stability. The reason behind this argument manifests itself when one examines the structural evolution of LNO under cycling. Evidently, a substantial contract of the c-lattice near the end of charge (SOC>~75%), i.e., due to H2-H3 phase transition,^[28–31] is universally demonstrated to be the leading cause to the structural degradation of LNO. What is worse is the oxygen evolution, despite under active debate over its underlying mechanisms and reversibility,^[24,30,32,33] accompanying the severe lattice distortion. While most studies^[28–30,34–36] employ *in situ*/operando X-ray diffraction to monitor the structural evolution of LNO (or Ni-rich cathodes), little attention is paid to the discussion of local Li/Ni environments, for example, Li/Ni–O bond lengths, as a function of Li content. This can be partially attributed to the relative insensitivity of X-ray to Li. From a structural point of view, however, it is of central importance to gain a comprehensive understanding beyond how the LNO crystal lattice behaves in response to Li⁺ de-/intercalation. It is expected that this information, with a focus on the H2-H3 phase transition and the single H3 phase region, could be potentially applied to Ni-rich and/or Co-free cathodes because they are closely related to the parent LNO structure.

[a] Dr. P.-H. Chien, X. Wu, Dr. B. Song, Dr. M. S. Everett, Dr. J. Liu

Neutron Scattering Division
Oak Ridge National Laboratory
Oak Ridge, TN 37830, USA
E-mail: liuj1@ornl.gov

[b] X. Wu, Dr. Z. Du
Electrification and Energy Infrastructures Division
Oak Ridge National Laboratory
Oak Ridge, TN 37830, USA
E-mail: duz1@ornl.gov

[c] X. Wu
School of Mechanical Engineering
Purdue University
West Lafayette, IN 47907, USA

[d] Z. Yang, C. K. Waters, Prof. F. Lin
Department of Chemistry
Virginia Tech
Blacksburg, VA 24061, USA

 Supporting information for this article is available on the WWW under <https://doi.org/10.1002/batt.202100135>

 An invited contribution to a joint Special Collection between Batteries & Supercaps and Chemistry-Methods on *In Situ* and Operando Methods for Energy Storage and Conversion.

Compared to X-ray/synchrotron diffraction, neutron diffraction offers several advantages: (1) The neutron scattering length of an element remains constant regardless of momentum transfer (Q). This property enables neutron diffraction to determine the position/occupancy of light elements such as Li with a high level of accuracy, (2) neutron penetrates into the bulk of materials without incurring heating, which prevents uneven electrochemical reactions when studying the structural evolution of both electrodes in a full cell is desired, and (3) the great contrast in scattering lengths between Li (-2.2 fm), Ni (10.3 fm), and O (5.8 fm) makes neutron diffraction an ideal probe to differentiate their positions in LNO during structural evolution. However, one must be reminded that the neutron flux is weaker than X-ray, not to mention synchrotron. Such intrinsic drawback requires excess loading of active materials (hundreds of milligrams) and longer acquisition time ($\sim 2\text{ hours}$ or more) to improve the statistics of a neutron powder diffraction (NPD) pattern. Also, the ^1H in the organic liquid electrolyte significantly dampens the signal of interest due to a large incoherent scattering length (25.3 fm). As a result, *in situ* operando neutron diffraction studies^[37–40] are rarely reported with detailed structural information other than crystal lattice of active materials.

The high flux neutron powder diffraction/total scattering instrument, Nanoscale Ordered Materials Diffractometer (NOMAD), at the Spallation Neutron Source (SNS), Oak Ridge National Laboratory, equips with high neutron flux ($\sim 1 \times 10^8\text{ neutrons cm}^{-2}\text{ sec}^{-1}$) and large detection coverage (4.0 steradian).^[41] This allows for rapid acquisition of NPD patterns with good quality for reliable parametric Rietveld refinements.^[42] Besides, a home-built electrochemical cell makes limited use of the organic liquid electrolyte, thereby minimizing unwanted interference of incoherent scattering from ^1H . In this work, we perform operando neutron diffraction study of a model system, i.e., $\text{LiNiO}_2||\text{graphite}$ full cell, on NOMAD with our newly designed cell configuration (Figure 1). We report detailed information on structural evolution of LiNiO_2 cathode (H1-M-H2-H3; H and M denotes hexagonal phase and monoclinic phase, respectively) and graphite anode ($\text{C} \leftrightarrow \text{LiC}_{24} \leftrightarrow \text{LiC}_{12} \leftrightarrow \text{LiC}_6$) in real time at C/10 (cycled between 2.8 V and 4.6 V). The abnormal change in both the Li/Ni–O bond lengths and $\text{LiO}_2/\text{NiO}_2$ layers thickness across the H2-H3 phase transition ($> \sim 85\%$ SOC) is identified and these anomalies are highly correlated with lattice distortion dictated by the oxygen z-coordinate. Finally, discussion of the unusual increase of the Ni–O bond length in the H3 phase is offered by considering the variation of Ni–O bond covalency as well as the concept of negative charge transfer between $\text{O}^{2-}(2\text{p})$ and $\text{Ni}^{4+}(3\text{d})$ orbitals.

2. Results and Discussion

2.1. Overview of Operando Neutron Diffraction Data of $\text{LiNiO}_2||\text{Graphite}$ Full Cell

High-resolution (Bank 5, $2\theta = 154^\circ$) operando neutron diffraction patterns of $\text{LiNiO}_2||\text{graphite}$ full cell for the first cycle are

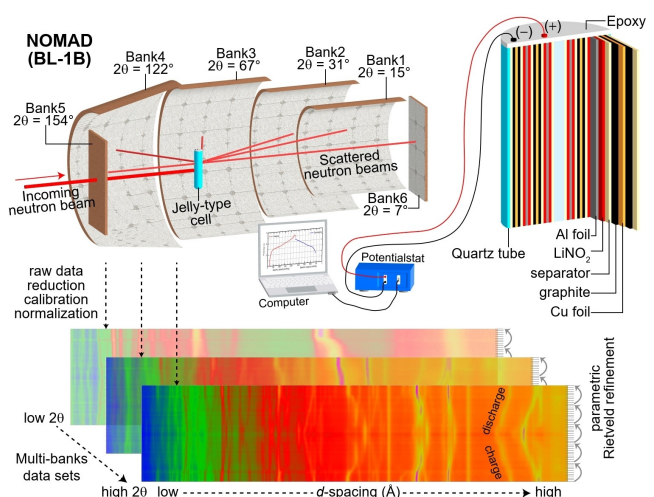


Figure 1. Schematic of operando neutron diffraction of $\text{LiNiO}_2||\text{graphite}$ full cell on the NOMAD (BL-1B) beamline at SNS, Oak Ridge National Laboratory. The jelly-type cell with detail cell configuration is shown on the top-right panel. Parametric Rietveld refinements are carried out with TOPAS(v6) on multiple-banks data sets, which are recorded in real time with the event of electrochemical cycling.

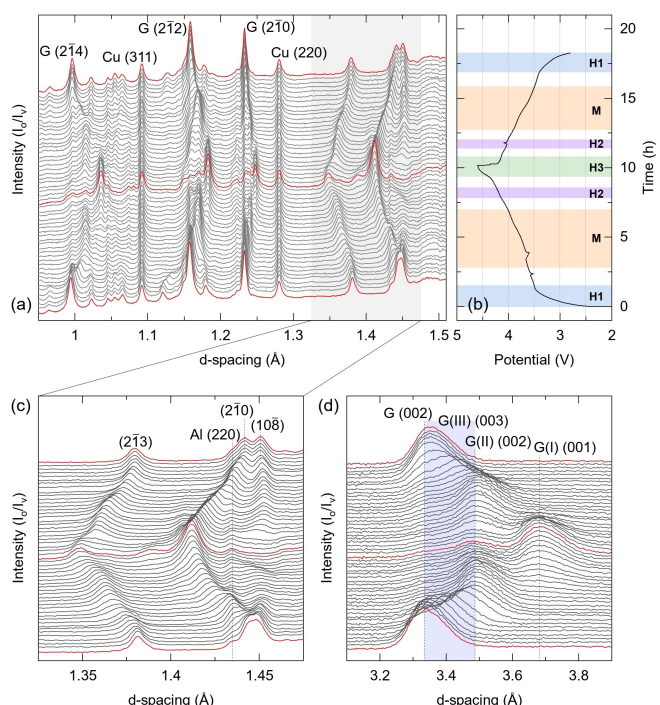


Figure 2. Operando neutron diffraction of $\text{LiNiO}_2||\text{graphite}$ full cell for the first cycle. a) High-resolution bank (Bank 5, $2\theta = 154^\circ$) neutron diffraction patterns. b) Voltage profile as a function of time. c) Selected diffraction patterns showing the evolution of Bragg reflections of Li_xNiO_2 . d) Selected diffraction patterns (Bank 2, $2\theta = 31^\circ$) showing the evolution of Bragg reflections of lithium-intercalated graphites (G: C_6 , G(III): stage III (LiC_{24}), G(II): stage II (LiC_{12}), and G(I): stage I (LiC_6)).

shown in Figure 2(a). The $\text{LiNiO}_2||\text{graphite}$ full cell is cycled at C/10 and its voltage profile (Figure 2b) is slightly smeared out in the absence of distinct plateaus^[22] to specify the two-phase (e.g., H2-H3) region^[29,30] (i.e., white areas in between single-

phase regions) in Li_xNiO_2 (Determination of cathode composition is described in the Supporting Information). Note that the small voltage fluctuation (drop or spike) is detected as a result of the inevitable vibration of the bracket which automatically changes the sample holder during operando operation. Accordingly, the two-phase regions are mapped out by comparing the evolution of *d*-spacings of a single phase (see Supporting Information). Overall, the obtained neutron diffraction patterns permit a clear identification of Bragg reflections of both cathode and anode components. For example, while the most intense Bragg reflections with *d*-spacing $< 1.3 \text{ \AA}$ can be assigned to Cu current collector ((220) and (311)) and graphite anode ((210), (212), and (214)), the Bragg reflections of Li_xNiO_2 cathode ((108), (210), and (213)) are shown in the high *d*-spacing ($> 1.3 \text{ \AA}$) region (see also Figure 2c).

For Li_xNiO_2 , the (210) reflection shifts to lower *d*-spacing upon charging, suggesting a continuous contraction of *ab* plane during the H1-M-H2-H3 phase transitions. The phenomenon of two-phase co-existence (e.g., H1-M solid-solution) agrees with literature results.^[29,30,43] By contrast, the (108) firstly migrates to higher *d*-spacing on the verge of the H2 phase region. The expanded *c*-lattice then shrinks abruptly once the H2-H3 phase transition kicks off as reflected by the shift of the (108) reflection toward a much lower *d*-spacing ($\sim 1.38 \text{ \AA}$ at the end of charge; see also Figure S1a). Reversible phase transitions, in the context of unavoidable production of spinel (LiNi_2O_4 or $\text{Li}_{0.5}\text{NiO}_2$)^[15,22,44] and rock-salt-type (NiO) phases,^[22,23,27] are observed upon discharging, yet a pronounced splitting of the (108) and (210) reflections appears after the first cycle (see Figure S1a). This implies a capacity loss which may relate to (1) the presence of Ni^{2+} in the Li interslab that minimizes the intercalation of Li^+ ,^[8,14] and (2) the build-up of solid electrolyte interphase (SEI) on the graphite anode.

In line with literature reports,^[37,45-47] multiple phase transitions of graphite anode are observed upon electrochemical cycling (Figure 2d). Upon charging, lithiation of graphite (G) continuously leads to the development of solid-solution phase (G(III): LiC_{24}),^[45,47,48] which is then converted to stage II phase (G(II): LiC_{12}). Further charging the $\text{LiNiO}_2||\text{graphite}$ full cell eventually yields the stage I phase (G(I): LiC_6) at the expense of the previously formed LiC_{12} via two-phase reaction.^[37] At the end of charge, a minor fraction of graphite remains un lithiated (see Figure S1b). The discharge process results in reversible phase transitions to a large extent, although the (002) reflection of graphite is not completely matched (i.e., *d*-spacing and peak intensity) before/after the first cycle. Therefore, it indicates that a very small amount of Li^+ , if not negligible, still persists in graphite anode.

2.2. Parametric Rietveld Refinements

Representative results (SOC = 0, 50%, 70%, 85%, 100%, and end of discharge) of parametric Rietveld refinements against the operando neutron diffraction data of $\text{LiNiO}_2||\text{graphite}$ full cell are displayed in Figure S2. Reasonable fits of all sets (53 in total) of diffraction data are obtained (Figure S3) for the first

cycle. Variations in both R_{wp} and G.O.F. (Goodness-Of-Fit) are inevitably noticed and they can be attributed to the evolution of two-phase co-existence regions (i.e., transition between two-phase region and single-phase region) for both Li_xNiO_2 cathode and graphite anode.

2.2.1. Graphite Anode

The coupling between the voltage profile of $\text{LiNiO}_2||\text{graphite}$ full cell and the graphite phase/lattice parameters evolution are shown in Figures S4 and S5. C_6 (G), LiC_{24} (G(III)), LiC_{12} (G(II)), and LiC_6 (G(I)) are employed to describe the structural evolution of the graphite anode. At SOC of 22% ($x=0.758$ in Li_xNiO_2), LiC_{24} starts to develop and reaches its maximal fraction at SOC of 37% ($x=0.623$ in Li_xNiO_2), which is then sacrificed for growing LiC_{12} . The transition from pristine C_6 to LiC_{24} (stage III) accompanies several non-stoichiometric Li_xC_6 phases (e.g., dilute stages)^[47,49,50] with specific stacking faults (i.e. faulting probability),^[51] and these issues are not incorporated into the parametric Rietveld refinements due to the complexity of data analysis and insufficient resolution of the current diffraction patterns. In addition, it is demonstrated that the formation of the dilute phase LiC_{30} (liquid stage II phase) depends heavily on Li^+ kinetics and a slower C-rate (at least $< \text{C}/10$; the C-rate used in the present work) is required for dilute phases to emerge.^[37,49] Likewise, the disappearance of LiC_{24} from neutron diffraction in charging a commercial 18650 cell at 1C is also documented.^[52] As a result, we avoid to explicitly describe a more sophisticated phase transition behavior due to the lack of high temporal resolution of our data. $\text{LiC}_{12} \rightarrow \text{LiC}_6$ phase transition occurs at SOC of 55% ($x=0.453$ in Li_xNiO_2) and is not complete at the end of charge, in which 14.8% of LiC_6 , 11.7% of LiC_{12} , and 2.7% of unreacted C_6 are detected. Upon cell discharging (i.e., charging the graphite anode), the evolution of phase transitions reverses its sequence and lithium-intercalated graphite are recovered at different stages. It is worth noting that nearly 100% of Li^+ is electrochemically pulled out from both LiC_{12} and LiC_6 (see Figure S1b) at the end of discharge. This indicates that the irreversible capacity ($\sim 41 \text{ mAh/g}$; $\sim 18\%$ active Li loss) results primarily from the loss of active Li due to the SEI formation in the first cycle. For reference, a $\sim 12\%$ capacity loss is typically observed in our jelly-type full cells after the first cycle.

2.2.2. Li_xNiO_2 Cathode

The lattice and volume evolution of Li_xNiO_2 upon de-/intercalation for the first cycle derived from parametric Rietveld refinements are shown in Figure 3. The refined monoclinic lattice parameters are transformed to the hexagonal setting for comparison.^[29] The onset of phase transitions (H1-M, M-H2, and H2-H3) in Li_xNiO_2 as compared to literature results^[29,30] using the second cycle for detailed Rietveld refinements, is slightly "lagged" at higher SOCs in the present work, which deals with the first cycle. The apparent inconsistency is likely due to

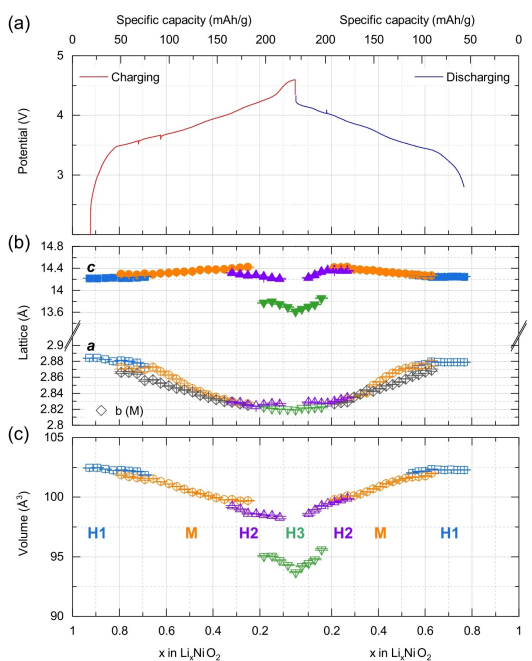


Figure 3. (a) Voltage profile of LiNiO_2 | graphite full cell as a function of Li content for the first cycle (specific capacity is shown at the top x-axis). (b) Evolution of lattice parameters (a and c) of Li_xNiO_2 as a function of Li content derived by parametric Rietveld refinements. For comparison, the obtained monoclinic lattice parameters (a_{M} , c_{M} , and β) were converted to hexagonal setting (a_{H} and c_{H}).^[29]

(1) the degree of the Li^+ /vacancy ordering that drives the phase transitions^[10,11] and (2) kinetically hindered phase transition in the first cycle.^[30,36,53] As expected, the c -lattice expands in the H1 and M phases during charging and it then decreases at SOC of ~70% ($x=0.318$ in Li_xNiO_2) upon the onset of the M-H2 phase transition. A significant decrease of the c -lattice (~85% SOC; $x=0.182$ in Li_xNiO_2) that initiates the collapse of the layered structure occurs during the H2-H3 phase transition, which is a well-known property for Ni-rich cathode materials.^[29-31,34,35,54] Indeed, the lattice volume experiences a similar fashion such that a sudden contraction of the crystal lattice (~3.7% from H2 to H3) is associated with the growth of the H3 phase during charging.^[29,30] On the contrary, the a -lattice continuously shrinks upon the removal of Li^+ from LiO_2 interslabs and it barely increases near the end of charge. Both the lattice and volume are reversibly attained upon discharging despite ~18% capacity loss.

The refined $\text{Li}/\text{Ni}-\text{O}$ bond lengths and $\text{O}-\text{Ni}-\text{O}$ angles (in-plane and out-of-plane) as a function of x in Li_xNiO_2 upon de-intercalation are summarized in Figure 4. The short-range structure of LiNiO_2 shows dynamic Jahn-Teller effect, i.e., there are four short $\text{Ni}-\text{O}$ bonds and two long $\text{Ni}-\text{O}$ bonds. However, the average structure of LiNiO_2 can be described using the space group (S.G.) $R-3m$ without long-range Jahn-Teller distortion, and this is due to the dynamic nature of the distortion. Therefore, an average $\text{Ni}-\text{O}$ bond lengths [(4 \times equatorial $\text{Ni}-\text{O}$ bond distances + 2 \times axial $\text{Ni}-\text{O}$ bond distances)/6] are plotted in Figure 4(b). At first glance, the dependency of $\text{Li}-\text{O}$ and $\text{Ni}-\text{O}$ bond length on electrochemical cycling

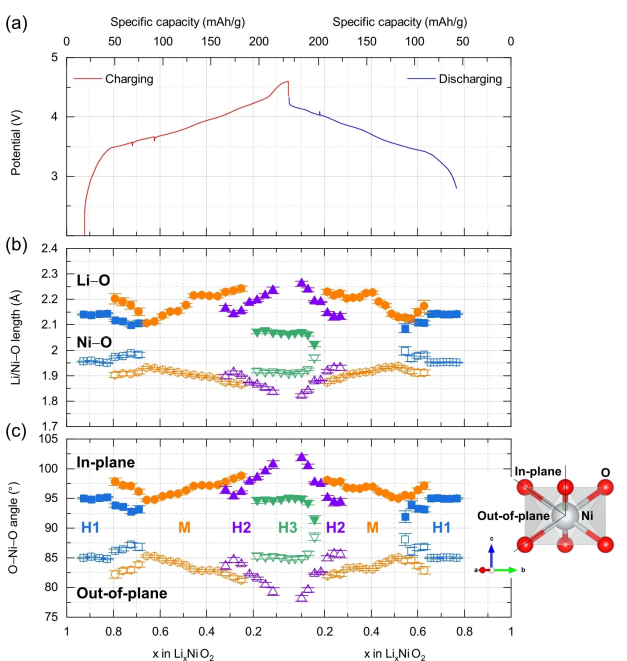


Figure 4. a) Voltage profile of LiNiO_2 | graphite full cell as a function of Li content for the first cycle (specific capacity is shown at the top x-axis). Evolution of b) $\text{Li}/\text{Ni}-\text{O}$ bond length and c) $\text{O}-\text{Ni}-\text{O}$ bond angles (in-plane and out-of-plane) of Li_xNiO_2 as a function of Li content derived by parametric Rietveld refinements.

follows a similar trend as revealed by crystal lattice parameters c and a , respectively. The increase(decrease) in $\text{Li}(\text{Ni})-\text{O}$ bond length echoes with, to a certain degree, the evolution of $c(a)$ -lattice upon charging. When Li re-intercalates into the NiO_2 host, reversible behavior is reasonably achieved. However, notable features are marked near the end of charge (~85% SOC; $x=0.182$ in Li_xNiO_2). First, the $\text{Li}-\text{O}$ bond length in the H2 phase keeps increasing instead of decreasing, as is illustrated in the case of the c -lattice as well as the lattice volume (Figure 3b,c). Second, the $\text{Ni}-\text{O}$ bond length in the H3 phase elongates abnormally and becomes longer than that in the H2 phase, whereas the a -lattice of the H2 and H3 phases is comparably close. The fact that the most evident reduction (promotion) of $\text{Li}(\text{Ni})-\text{O}$ bond length is found in the H3 phase suggests that the highly delithiated H3 phase is mainly responsible for the collapse of layered structure. Consequently, this confirms that the improvement of capacity retention of LiNiO_2 cathode (and Ni-rich cathode materials) can be achieved by controlling the upper cutoff voltage^[26,31,34] to intentionally mitigate the formation of the H3 phase.

Alternatively, the $\text{O}-\text{Ni}-\text{O}$ angles can be viewed as an indicator to examine the local distortion of the NiO_6 octahedra. The deviation of the $\text{O}-\text{Ni}-\text{O}$ angles from 90° can be observed and opposite developments between the in-plane and out-of-plane angles continue to evolve with charging (Figure 3b). This certainly reflects that the NiO_2 slabs are compressed, i.e., highly distorted, along with delithiation. In striking contrast, the “compression” in the Li^+ -depleted H3 phase (~85% SOC; $x=0.182$ in Li_xNiO_2) is released such that its in-plane and out-of-

plane O–Ni–O angles are almost in line with the level of distortion detected in the H1 phase (highly lithiated).

Along the same lines, the thickness of LiO_2 interlayers and NiO_2 slabs (Figure 5) mirrors the behaviors of the structural evolution surveyed by the Li/Ni–O bond lengths and the O–Ni–O angles. Indeed, these observations (including a - and c -lattice) are coupled in a sense that they are all governed by the oxygen z -coordinate (O_z) (Figure 5c). In the same way, the change of O–O_{interlayer} distance (Figure 6) in the NiO_6 octahedra is greatly synchronized with the evolution of the NiO_2 slabs thickness. While lowering the value of O_z during charging typically drives the shrinkage of the NiO_2 slabs since the Ni–O bond shortens concomitantly, the scenario is conversely played out for the Li–O bond in the LiO_6 octahedra, and hence the expansion of the LiO_2 interlayers. On one hand, the decreasing of the NiO_2 slabs thickness (and hence the Ni–O bond length) throughout the phase transitions (H1–M–H2) can be understood in the context of oxidation of nickel from 3+ (ionic radius: 0.56 Å; low spin) to 4+ (ionic radius: 0.48 Å).^[55] In addition, Li^+ de-intercalation causes the increase of the Ni–O bond covalency, which reduces the Ni–O bond length.^[56,57] On the other hand, it is commonly accepted that the removal of Li^+ from the LiO_2 interlayers discounts the screening effect of Li^+ on O^{2-} ; therefore, the repulsion that originates from negative charges on oxygen increases, yielding the observed expansion of the LiO_2 interlayers. In short, the alleviated screening effect by Li^+ and enhanced Ni–O bond covalency cooperatively exert the influence over the structural evolution of Li_xNiO_2 upon de-/lithiation, which, in turn, alters the observed change in the LiO_2 (interslabs)/ NiO_2 (slabs) thickness. However, the anomaly in O_z

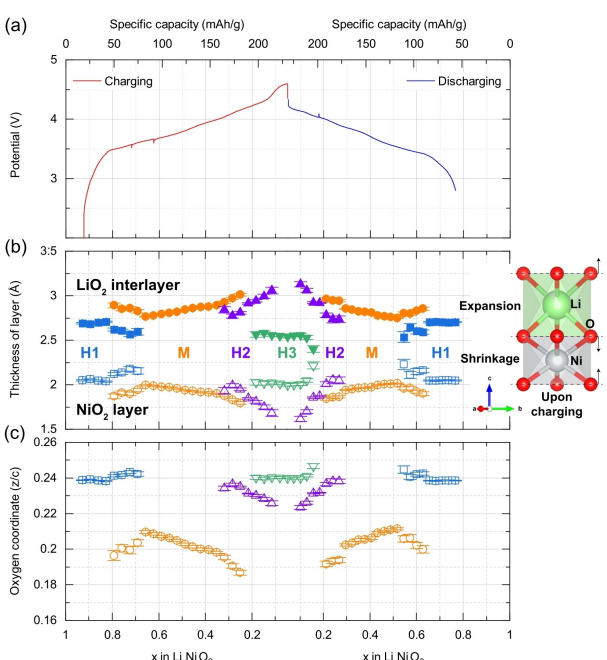


Figure 5. a) Voltage profile of LiNiO_2 | graphite full cell as a function of Li content for the first cycle (specific capacity is shown at the top x-axis). Evolution of b) LiO_2 interslab thickness and c) NiO_2 slab thickness as a function of Li content derived by parametric Rietveld refinements.

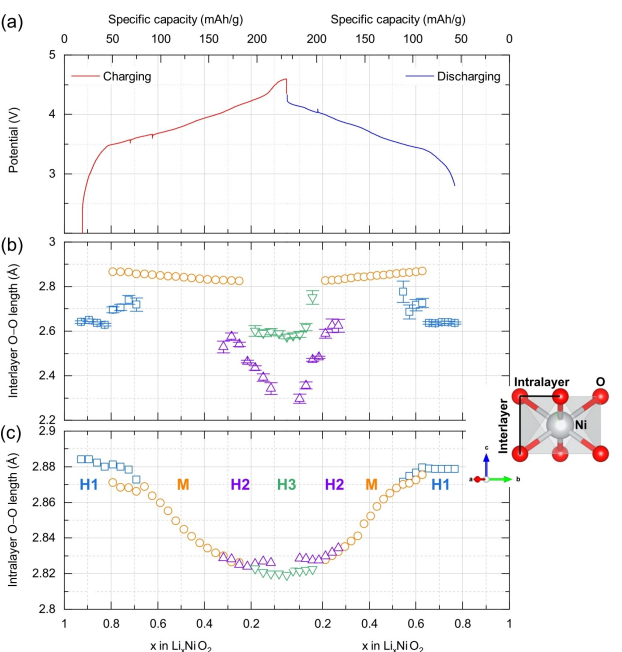


Figure 6. a) Voltage profile of LiNiO_2 | graphite full cell as a function of Li content for the first cycle (specific capacity is shown at the top x-axis). Evolution of b) interlayer O–O length and c) intralayer O–O length as a function of Li content derived by parametric Rietveld refinements. The evolution of O–O_{intralayer} distance basically follows the same trend as illustrated in the a -lattice (cf. Figure 3).

upon H2–H3 phase transition at SOC of ~85 % during charging leads to a decrease, instead of an intuitively expected increase, in the LiO_2 interslab thickness (NiO_2 slab shows the opposite trend).

The abnormal rise of the Ni–O bond length at high levels of delithiation ($x < \sim 0.2$ in Li_xNiO_2 in the present work) is also identified in a recent work^[30] (by X-ray diffraction) and our previous investigations of Ni-rich cathode materials such as NMC811 or NCA.^[58,59] Conventionally, the average Ni–O bond lengths are expected to decrease during charging because of the decrease of ionic radii and the increase of the Ni–O covalency. This agrees well with the observations during the first two transitions (e.g., H1–M and M–H2). Similar finding has been, for example, demonstrated in LiCoO_2 cathode material and the decrease of the Co–O bond covalency (upon delithiation) was experimentally confirmed by O K-edge X-ray absorption spectroscopy^[60] and DFT calculations.^[56] However, the abnormal increase of the Ni–O bond length in the H3 phase is more likely triggered by another driving force other than the Ni–O bond covalency alone.

Specifically, we noticed that the negative charge transfer^[34,56,60,61] has been linked to the anomalous change in the Ni–O bond length. For example, an abnormal increase of the Ni–O bond length was captured in $\text{La}_{2-x}\text{Sr}_x\text{NiO}_4$ when x is larger than 1.4.^[62] It is worth mentioning that the nominal oxidation state of nickel gradually approaches 4+ with increasing x in $\text{La}_{2-x}\text{Sr}_x\text{NiO}_4$ and, by analogy, this simulates the situation of local environment of Ni^{4+} in the highly delithiated Li_xNiO_2 . Historically, this phenomenon can be explained by the

negative charge transfer between oxygen 2p orbital and nickel 3d orbital that induces partial charge transfer from the filled 2p bands in oxygen to the strongly p-d hybridized states with predominant Ni 3d parentage. The pioneering work by Rao et al.^[63] has even suggested that the oxidation state of nickel in LiNiO₂ should be treated as 2+ since, via O 1s and Ni 2p_{3/2} X-ray photoelectron spectroscopy, they claimed electron holes are created on oxygen by $\text{Ni}^{3+} + \text{O}^{2-} \leftrightarrow \text{Ni}^{2+} + \text{O}^-$. In other words, an electron hole can be created on oxygen by donating an electron from π^* states (2p dominant) to σ^* states (strong d-p hybridization). Likewise, La_{2-x}Sr_xCuO₄^[64] also shows significant hole character on oxygen 2p orbitals when the concentration of Sr increases. Taken together, charge compensation in part leads to the collapse of the c-lattice (LiO₂ interslabs) when the H3 phase emerges because the reduced charge concentration on oxygen eventually minimizes the coulombic repulsion that initially takes place upon de-intercalation of Li⁺ from Li_xNiO₂.

Of more profound importance to the charge compensation is, as suggested by Goodenough et al.,^[62] the $\text{Ni}^{4+} + \text{O}^{2-} \leftrightarrow \text{Ni}^{3+} + \text{O}^-$ equilibrium, which hypothetically implies that the Ni–O rehybridization upon de-intercalation of Li⁺ could keep the average oxidation state of nickel to 3+, i.e., the equilibrium tends to shift to the right. Indeed, first-principles prediction of Li_xCoO₂ cathode confirms that the calculated positive charge density on cobalt is nearly identical regardless of Li content, e.g., LiCoO₂, Li_{0.5}CoO₂, or CoO₂.^[65] Zunger et al.^[66] further employs first-principles quantum mechanical calculations to reveal that this “charge self-regulation” generally responds to the change of oxidation state of a transition metal (TM), cf., removing Li⁺ from Li_xNiO₂, and a constant TM charge is recognized. De-lithiating Li_xNiO₂ (>~85% SOC in the present work) most likely places the energy level of the empty 3d band (e_g dominant) of Ni⁴⁺ lower than that of the 2p band of O²⁻. In this oversimplified scenario, a negative charge transfer ($\Delta\text{CT} < 0$) could happen in favor of Ni⁴⁺(3d)–O²⁻(2p) rehybridization. Consequently, the low-lying bonding level substantially features Ni components occupied by electrons, whereas the anti-bonding level is more characterized by oxygen (2p orbital) enriched with holes.^[67] It is also possible that a new intermediate hybridized state, similar to the polaron state, may form between the two major bands through rehybridization at high degrees of delithiation.^[68] These arguments, of course, will need more insights from detailed calculations, specifically tailored for LiNiO₂ cathode system to verify the complicated electronic structure involving the dynamic change of rehybridization between Ni (3d) and O (2p) atoms under electrochemical cycling. We should also stress that a similar situation (negative charge transfer) has also been reported in other materials including spinel (LiNi_xMn_{2-x}O₄),^[69] nickelate (NdNiO₃),^[70] and a transition-metal halide (Cs₂Au₂Cl₆).^[71] Therefore, it is believed that the structural anomaly, i.e., the collapse of the c-lattice near the end of charge, in Ni-rich cathode materials can be broadly attributed to the complex multiple effects as discussed above.

3. Conclusions

We carried out the operando neutron diffraction on a home-built jelly-type LiNiO₂ | graphite full cell charging/discharging at C/10 for the first cycle. Quantitative analysis is successfully performed using parametric Rietveld refinement to monitor the structural evolution of both Li_xNiO₂ cathode and graphite anode. Detailed information on structural changes including crystal lattice, Li/Ni–O bond lengths, LiO₂(interslabs)/NiO₂(slabs) thickness, and O–Ni–O bond angles are discussed and reported for the first time. In particular, the abnormal variation of the Ni–O bond length in the H3 phase at high SOC (>~85% in this work) is explained by a simplified scheme (negative charge transfer). It is believed that the commonly observed unusual structural evolution of Ni-rich cathode materials can be justified by the effect of negative charge transfer as well.

Experimental Section

Experimental details are described in the Supporting Information.

Acknowledgements

Research conducted at the NOMAD beamlines at ORNL's Spallation Neutron Source was sponsored by the Scientific User Facilities Division, Office of Basic Sciences, U.S. Department of Energy. This research at Oak Ridge National Laboratory, managed by UT Battelle, LLC, for the U.S. Department of Energy (DOE) under contract DE-AC05-00OR22725, was sponsored by the Office of Energy Efficiency and Renewable Energy (EERE) and Vehicle Technologies Office (VTO). The work at Virginia Tech is supported by the U.S. Department of Energy's Office of Energy Efficiency and Renewable Energy (EERE) under the award number: DE-EE0008444 (Technology Manager: Peter Faguy).

Conflict of Interest

The authors declare no conflict of interest.

Keywords: LiNiO₂ · lithium-ion batteries · operando neutron diffraction · phase transition · structural evolution

- [1] J. Deng, C. Bae, A. Denlinger, T. Miller, *Joule* **2020**, *4*, 511–515.
- [2] A. Masias, J. Marcicki, W. A. Paxton, *ACS Energy Lett.* **2021**, *6*, 621–630.
- [3] B. Dunn, H. Kamath, J.-M. Tarascon, *Science* **2011**, *334*, 928–935.
- [4] L. D. Dyer, B. S. Borie Jr., G. P. Smith, *J. Am. Chem. Soc.* **1954**, *76*, 1499–1503.
- [5] Y. M. Gulyamov, M. D. Dolgushin, V. P. Morozov, L. N. Sagoyan, *Elektrokhimiya* **1971**, *7*, 896–899.
- [6] A. Yoshino, K. Sanечika, T. Nakajima, *Secondary Batteries*, **1985**, US4668595A.
- [7] K. Mizushima, P. C. Jones, P. J. Wiseman, J. B. Goodenough, *Mater. Res. Bull.* **1980**, *15*, 783–789.
- [8] J. P. Peres, C. Delmas, P. Biensan, P. Willmann, *J. Phys. Chem. Solids* **1996**, *57*, 1057–1060.

- [9] R. Kanno, H. Kubo, Y. Kawamoto, *J. Solid State Chem.* **1994**, *110*, 216–225.
- [10] C. Pouillerie, E. Suard, C. Delmas, *J. Solid State Chem.* **2001**, *158*, 187–197.
- [11] J. P. Peres, F. Weill, C. Delmas, *Solid State Ionics* **1999**, *116*, 19–27.
- [12] T. Ohzuku, A. Ueda, M. Nagayama, *J. Electrochem. Soc.* **1993**, *140*, 1862–1870.
- [13] J. R. Dahn, U. von Sacken, C. A. Michal, *Solid State Ionics* **1990**, *44*, 87–97.
- [14] H. Arai, S. Okada, Y. Sakurai, J.-I. Yamaki, *Solid State Ionics* **1997**, *95*, 275–282.
- [15] H. Arai, S. Okada, Y. Sakurai, J. Yamaki, *Solid State Ionics* **1998**, *109*, 295–302.
- [16] J. R. Dahn, M. Obrovac, *Solid State Ionics* **1994**, *69*, 265–270.
- [17] H.-J. Noh, S. Youn, C. S. Yoon, Y.-K. Sun, *J. Power Sources* **2013**, *233*, 121–130.
- [18] W. Li, E. M. Erickson, A. Manthiram, *Nat. Energy* **2020**, *5*, 26–34.
- [19] H. Li, M. Cormier, N. Zhang, J. Inglis, J. Li, J. R. Dahn, *J. Electrochem. Soc.* **2019**, *166*, A429–A439.
- [20] R. Weber, H. Li, W. Chen, C.-Y. Kim, K. Plucknett, J. R. Dahn, *J. Electrochem. Soc.* **2020**, *167*, 100501.
- [21] N. Zhang, J. Stark, H. Li, A. Liu, Y. Li, I. Hamam, J. R. Dahn, *J. Electrochem. Soc.* **2020**, *167*, 080518.
- [22] T. Deng, X. Fan, L. Cao, J. Chen, S. Hou, X. Ji, L. Chen, S. Li, X. Zhou, E. Hu, D. Su, X.-Q. Yang, C. Wang, *Joule* **2019**, *3*, 2550–2564.
- [23] C. Wang, L. Han, R. Zhang, H. Cheng, L. Mu, K. Kisslinger, P. Zou, Y. Ren, P. Cao, F. Lin, H. L. Xin, *Matter* **2021**, *4*, 2013–2026.
- [24] F. Kong, C. Liang, L. Wang, Y. Zheng, S. Peramanthan, R. C. Longo, J. P. Ferraris, M. Kim, K. Cho, *Adv. Energy Mater.* **2019**, *9*, 1802586.
- [25] J. Xu, F. Lin, D. Nordlund, E. J. Crumlin, F. Wang, J. Bai, M. M. Doeffer, W. Tong, *Chem. Commun.* **2016**, *52*, 4239–4242.
- [26] C. S. Yoon, D.-W. Jun, S.-T. Myung, Y.-K. Sun, *ACS Energy Lett.* **2017**, *2*, 1150–1155.
- [27] S. Ahmed, M. Bianchini, A. Pokle, M. S. Munde, P. Hartmann, T. Brezesinski, A. Beyer, J. Janek, K. Volz, *Adv. Energy Mater.* **2020**, *10*, 2001026.
- [28] W. Li, J. N. Reimers, J. R. Dahn, *Solid State Ionics* **1993**, *67*, 123–130.
- [29] H. Li, N. Zhang, J. Li, J. R. Dahn, *J. Electrochem. Soc.* **2018**, *10*, 050506.
- [30] L. de Biasi, A. Schiele, M. Roca-Ayats, G. Garcia, T. Brezesinski, P. Hartmann, J. Janek, *ChemSusChem* **2019**, *12*, 2240–2250.
- [31] H. Li, A. Liu, N. Zhang, Y. Wang, S. Yin, H. Wu, J. R. Dahn, *Chem. Mater.* **2019**, *31*, 7574–7583.
- [32] J. Cheng, L. Mu, C. Wang, Z. Yang, H. L. Xin, F. Lin, K. A. Persson, *J. Mater. Chem. A* **2020**, *8*, 23293–23303.
- [33] D. Choi, J. Kang, B. Han, *Electrochim. Acta* **2019**, *294*, 166–172.
- [34] A. O. Kondrakov, H. Geßwein, K. Galdina, L. de Biasi, V. Meded, E. O. Filatova, G. Schumacher, W. Wenzel, P. Hartmann, T. Brezesinski, J. Janek, *J. Phys. Chem. C* **2017**, *121*, 24381–24388.
- [35] C. Xu, K. Märker, J. Lee, A. Mahadevogowda, P. J. Reeves, S. J. Day, M. F. Groh, S. P. Emge, C. Ducati, B. Layla Mehdi, C. C. Tang, C. P. Grey, *Nat. Mater.* **2021**, *20*, 84–92.
- [36] A. Grenier, P. J. Reeves, H. Liu, I. D. Seymour, K. Märker, K. M. Wiaderek, P. J. Chupas, C. P. Grey, K. W. Chapman, *J. Am. Chem. Soc.* **2020**, *142*, 7001–7011.
- [37] S. Taminato, M. Yonemura, S. Shiotani, T. Kamiyama, S. Torii, M. Nagao, Y. Ishikawa, K. Mori, T. Fukunaga, Y. Onodera, T. Naka, M. Morishima, Y. Ukyo, D. S. Adipranoto, H. Arai, Y. Uchimoto, Z. Ogumi, K. Suzuki, M. Hirayama, R. Kanno, *Sci. Rep.* **2016**, *6*, 28843.
- [38] L. Vitoux, M. Reichardt, S. Sallard, P. Novák, D. Sheptyakov, C. Villevieille, *Front. Energy Res.* **2018**, *6*, 76.
- [39] H. Liu, C. R. Fell, K. An, L. Cai, Y. S. Meng, *J. Power Sources* **2013**, *240*, 772–778.
- [40] F. Rosciano, M. Holzapfel, W. Scheifele, P. Novák, *J. Appl. Crystallogr.* **2008**, *41*, 690–694.
- [41] S. Calder, K. An, R. Boehler, C. R. Dela Cruz, M. D. Frontzek, M. Guthrie, B. Haberl, A. Huq, S. A. J. Kimber, J. Liu, J. J. Molaison, J. Neufeld, K. Page, A. M. dos Santos, K. M. Taddei, C. Tulk, M. G. Tucker, *Rev. Sci. Instrum.* **2018**, *89*, 092701.
- [42] G. W. Stinton, J. S. O. Evans, *J. Appl. Crystallogr.* **2007**, *40*, 87–95.
- [43] M. Bianchini, M. Roca-Ayats, P. Hartmann, T. Brezesinski, J. Janek, *Angew. Chem. Int. Ed.* **2019**, *58*, 10434–10458; *Angew. Chem.* **2019**, *131*, 10542–10569.
- [44] M. G. S. R. Thomas, W. I. F. David, J. B. Goodenough, P. Groves, *Mater. Res. Bull.* **1985**, *20*, 1137–1146.
- [45] J. R. Dahn, R. Fong, M. J. Spoon, *Phys. Rev. B* **1990**, *42*, 6424–6432.
- [46] K. P. C. Yao, J. S. Okasinski, K. Kalaga, I. A. Shkrob, D. P. Abraham, *Energy Environ. Sci.* **2019**, *12*, 656–665.
- [47] T. Ohzuku, Y. Iwakoshi, K. Sawai, *J. Electrochem. Soc.* **1993**, *140*, 2490–2498.
- [48] J. R. Dahn, *Phys. Rev. B* **1991**, *44*, 9170–9177.
- [49] C. Didier, W. K. Pang, Z. Guo, S. Schmid, V. K. Peterson, *Chem. Mater.* **2020**, *32*, 2518–2531.
- [50] T. Yao, *Solid State Ionics* **2004**, *175*, 199–202.
- [51] R. E. Johnsen, P. Norby, M. Leoni, *J. Appl. Crystallogr.* **2018**, *51*, 998–1004.
- [52] X.-L. Wang, K. An, L. Cai, Z. Feng, S. E. Nagler, C. Daniel, K. J. Rhodes, A. D. Stoica, H. D. Skorpenske, C. Liang, W. Zhang, J. Kim, Y. Qi, S. J. Harris, *Sci. Rep.* **2012**, *2*, 747.
- [53] H. Zhou, F. Xin, B. Pei, M. S. Whittingham, *ACS Energy Lett.* **2019**, *4*, 1902–1906.
- [54] K. Märker, P. J. Reeves, C. Xu, K. J. Griffith, C. P. Grey, *Chem. Mater.* **2019**, *31*, 2545–2554.
- [55] R. D. Shannon, *Acta Crystallogr.* **1976**, *A32*, 751–767.
- [56] D.-H. Seo, A. Urban, G. Ceder, *Phys. Rev. B* **2015**, *92*, 115118.
- [57] Y. Koyama, T. Mizoguchi, H. Ikeno, I. Tanaka, *J. Phys. Chem. B* **2005**, *109*, 10749–10755.
- [58] J. Liu, Z. Du, X. Wu, L. Geng, B. Song, P.-H. Chien, M. S. Everette, unpublished results.
- [59] X. Wu, B. Song, P.-H. Chien, M. S. Everette, K. Zhao, J. Liu, Z. Du, unpublished results.
- [60] W.-S. Yoon, K.-B. Kim, M.-G. Kim, M.-K. Lee, H.-J. Shin, J.-M. Lee, J.-S. Lee, C.-H. Yo, *J. Phys. Chem. B* **2002**, *106*, 2526–2532.
- [61] Z. W. Lebens-Higgins, N. V. Faenza, M. D. Radin, H. Liu, S. Sallis, J. Rana, J. Vinckeviciute, P. J. Reeves, M. J. Zuba, F. Badway, N. Pereira, K. W. Chapman, T.-L. Lee, T. Wu, C. P. Grey, B. C. Melot, A. Van Der Ven, G. G. Amatucci, W. Yang, L. F. J. Piper, *Mater. Horiz.* **2019**, *6*, 2112–2123.
- [62] Y. Takeda, R. Kanno, M. Sakano, O. Yamamoto, M. Takano, Y. Bando, H. Akinaga, K. Takita, J. B. Goodenough, *Mat. Res. Bull.* **1990**, *25*, 293–306.
- [63] G. R. Rao, D. D. Sarma, C. N. R. Rao, *J. Phys. Condens. Matter* **1989**, *1*, 2147–2150.
- [64] T. Kamiyama, F. Izumi, H. Asano, H. Takagi, S. Uchida, Y. Tokura, E. Takayama-Muromach, M. Matsuda, K. Yamada, Y. Endoh, Y. Hidaka, *Physica C* **1990**, *172*, 120–126.
- [65] C. Wolverton, A. Zunger, *Phys. Rev. Lett.* **1998**, *81*, 606–609.
- [66] H. Raebiger, S. Lany, A. Zunger, *Nature* **2008**, *453*, 763–766.
- [67] A. E. Bocquet, T. Mizokawa, T. Saitoh, H. Namatame, A. Fujimori, *Phys. Rev. B* **1992**, *46*, 3771.
- [68] Q. Liu, G. M. Dalpian, A. Zunger, *Phys. Rev. Lett.* **2019**, *122*, 106403.
- [69] H. Liu, J. Zhou, L. Zhang, Z. Hu, C. Kuo, J. Li, Y. Wang, L. H. Tjeng, T.-W. Pi, A. Tanaka, L. Song, J.-Q. Wang, S. Zhang, *J. Phys. Chem. C* **2017**, *121*, 16079–16087.
- [70] V. Bisogni, S. Catalano, R. J. Green, M. Gibert, R. Scherwitzl, Y. Huang, V. N. Strocov, P. Zubko, S. Balandeh, J.-M. Triscone, G. Sawatzky, T. Schmitt, *Nat. Commun.* **2016**, *7*, 13017.
- [71] A. V. Ushakov, S. V. Streletsov, D. I. Khomskii, *J. Phys. Condens. Matter* **2011**, *23*, 445601.

Manuscript received: June 21, 2021

Revised manuscript received: July 22, 2021

Version of record online: September 8, 2021